A comparative investigation on the effects of nitrogen-doping into graphene on enhancing the electrochemical performance of SnO₂/graphene for sodium-ion batteries†

Xiuqiang Xie,*[a] Dawei Su,[a] Jinqiang Zhang,[a] Shuangqiang Chen,[a] Anjon Kumar Mondal[a] and Guoxiu Wang*[a,b]

SnO₂/nitrogen-doped graphene nanohybrids have been synthesized by an *in situ* hydrothermal method, during which the formation of SnO₂ nanocrystals and nitrogen doping of graphene occur simultaneously. The as-prepared SnO₂/nitrogen-doped graphene nanohybrids exhibit enhanced electrochemical performance for sodium-ion batteries compared to SnO₂/graphene nanocomposites. A systematic comparison between SnO₂/nitrogen-doped graphene nanohybrids and the SnO₂/graphene counterpart as anode materials for sodium-ion batteries has been conducted. The comparison is in a reasonable framework, where SnO₂/nitrogen-doped graphene nanohybrids and the SnO₂/graphene counterpart have the same SnO₂ ratio, similar SnO₂ crystallinity and particle size, close surface area and pore size. The results clearly manifest that the improved electron transfer efficiency of SnO₂/nitrogen-doped graphene due to nitrogen-doping plays a more important role than the increased electro-active sites within graphene network in enhancing the electro-activity of SnO₂/nitrogen-doped graphene nanohybrids compared to the SnO₂/graphene counterpart. In contrast to the previous reports which often ascribe the enhanced electro-activity of nitrogen-doped graphene based composites to two nitrogen-doping effects (improving the electron transfer efficiency and increasing electro-active sites within graphene networks) in one single declaration, this work is expected to provide more specific information for understanding the effects of nitrogen-doping into graphene on improving the electrochemical performance of graphene based composites.

Introduction

The global distribution of lithium and the future capital investment in lithium usage would make lithium-ion batteries (LIBs) costly for the large-scale applications. The rich sodium source makes sodium-ion batteries (SIBs) a sustainable and

economically attractive electrochemical energy conversion and storage technique in the long term, which can be used as a near-term substitution for LIBs.[1–7] To support the practical applications of SIBs, one critical issue is to develop electrode materials with the capability for fast and stable sodium ion storage.[8,9]

Carbon materials have been applied as scaffolds to support Na-ion host materials, such as phosphorous,[10–12] Sn-based compounds,[4,6,13–16] and Sb-based materials,[17,18] in order to increase the electronic conductivity and buffer the volume change of electrode materials during charge/discharge processes. Graphene has been widely used as effective building blocks for these purposes, owing to its high electronic conductivity, two-dimensional structure with high surface area, and flexibility.[14,15,19–26] In order to meet the demand of high energy storage, numerous efforts have been devoted to enhancing the electrochemical performance of the graphene-based composite materials based on rational material manipulations. Chemical substitution of graphene by heteroatoms, such as B, N, and S, could bring new physicochemical functionalities.[27–30] It is rife that the doping of graphene

[a]*Centre for Clean Energy Technology, School of Chemistry and Forensic Science, University of Technology Sydney, Broadway, Sydney, NSW 2007, Australia. E-mail: xiexiuqiang@gmail.com, Guoxiu.Wang@uts.edu.au; Fax: +61 2 95141460; Tel: +61 2 95141741*

[b]*College of Materials Science & Engineering, Nanjing University of Aeronautics and Astronautics, Nanjing, P.R. China*

†Electronic supplementary information (ESI) available: Schematic illustration for the preparation of SnO₂/NG nanocomposite, TGA curves of SnO₂/G and SnO₂/NG, N₂ sorption isotherms of SnO₂/G and SnO₂/NG composites, CV profiles of NG at a scan rate of 0.1 mV s⁻¹ between 0.01 and 3.0 V, charge–discharge curves of bare SnO₂ at a current density of 20 mA g⁻¹, galvanostatic charge–discharge profiles of the SnO₂/NG and SnO₂/G composites of the 50th cycle and 100th cycle at 20 mA g⁻¹, SEM images of SnO₂/NG electrode after 100 cycles, kinetic parameters of SnO₂/G and SnO₂/NG electrodes. See DOI: 10.1039/c4nr07054b

matrix by nitrogen heteroatoms can improve the electrochemical performance for Na$^+$ storage.[31–33] For example, Kang and co-workers have reported the enhanced electrochemical performance for SIBs in TiO$_2$/nitrogen-doped graphene nanocomposites with open pore channel compared to TiO$_2$/graphene counterparts.[32] Qin *et al.* found nitrogen-dopants in graphene can restrict further structural growth and result in smaller size of TiO$_2$, which contributes to the improved capacity and rate capability of TiO$_2$/nitrogen-doped graphene compared to TiO$_2$/graphene for SIBs.[33] However, to manifest the inherent nitrogen-doping effects for enhancing the sodium-ion storage performance, a logical comparison between nitrogen-doped graphene based nanocomposites and the nitrogen-free ones should be in a reasonable framework excluding: (1) the difference of the loading ratio of supported materials in the compared composites, (2) the possible morphology effects, such as the crystallinity and particle size of supported materials, the surface area of the composites determining the electrode/electrolyte contact. In this aspect, a rational and systematic comparison between nitrogen-doped graphene based nanocomposites and the nitrogen-free ones for Na$^+$ storage has been still unavailable. On the other hand, the previous reports available in this area often attribute the enhanced electroactivity of the nitrogen-doped graphene (NG) based nanocomposites to the increased electro-active sites within graphene networks and the improvement of electron transfer efficiency of the overall electrode due to nitrogen-doping.[32,34] Nevertheless, the contribution ratio of each effect to the overall capacity enhancement is still ambiguous.

Herein, we choose SnO$_2$ as a typical example to investigate the intrinsic nitrogen-doping effects for improving the sodium-ion storage in the graphene-based nanocomposites. An *in situ* hydrothermal route was used to prepare SnO$_2$/nitrogen-doped graphene (SnO$_2$/NG) nanohybrids as anode materials for SIBs. For comparison, SnO$_2$/graphene (SnO$_2$/G) nanohybrids with the same SnO$_2$ weight ratio were prepared by the similar procedure without nitrogen-doping agents. The results indicate that the particular characteristics in these two series of composites including the crystallinity, the particle size, and the morphology of SnO$_2$ are identical. Based on such a desirable system, a comparison between SnO$_2$/NG and SnO$_2$/G featuring analogous morphology as anode materials for SIBs has been conducted. The as-prepared SnO$_2$/NG electrode exhibits a higher sodium-ion storage capacity than the SnO$_2$/G counterpart. In particular, by controlled experiments using bare NG and graphene as anode materials for SIBs, we find that the improved electron transfer efficiency due to nitrogen-doping has an important contribution to the observed enhanced electrochemical performance; whereas the increased electro-active sites within graphene networks benefiting from nitrogen-doping has limited contribution to the overall electrochemical performance enhancement. This work could provide more specific information for understanding the effects of nitrogen-doping into graphene on improving the electrochemical performance of graphene based composites.

Experimental

Materials

Graphene oxide (GO) nanosheets were synthesized from natural graphite powders by a modified Hummer's method.[35] SnO$_2$/G and SnO$_2$/NG composites were produced by a hydrothermal method. Typically, SnCl$_4$·5H$_2$O (40 mg, Sigma-Aldrich, ≥98%) was mixed with GO aqueous suspension (40 mL, 1 mg mL^{-1}) by ultrasonication using a Branson Digital Sonifier (S450D, 40% amplitude). After ultrasonication for 1 h, the mixture was divided into two parts (20 mL each). To prepare SnO$_2$/NG nanohybrids, urea (5 g) was added to one part and stirred for 30 min. Both solutions were then heated to 180 °C in a Teflon-lined autoclave (25 mL in capacity) and maintained at that temperature for 24 h. The precipitates were cooled to room temperature naturally, and then collected and washed with distilled water and ethanol several times. After drying at 60 °C in a vacuum oven overnight, the final products were obtained.

Structural and physical characterization

The crystal structure and phases of as-prepared materials were characterized by X-ray diffraction (XRD, Siemens D5000) using a Cu Kα radiation at a scanning step of 0.02° s^{-1}. The morphology was analyzed by field emission scanning electron microscope (FESEM, Zeiss Supra 55VP). The crystal structure details were further characterized by transmission electron microscopy (TEM) and high-resolution transmission electron microscopy (HRTEM, JEOL JEM-2011). Simultaneous thermalgravimetric analysis and differential thermal analysis (TGA/DTA) were performed with a 2960 SDT system to analyze the weight ratio of SnO$_2$ at a heating rate of 10 °C min^{-1} in air from room temperature to 800 °C. The XPS spectra were carried out on an ESCALAB 250Xi XPS System with a monochromated Al Kα X-ray source (13 kV 150 W 500 μm with pass energy of 100 eV for survey scans, or 20 eV for region scans). All of the binding energies were calibrated by C 1s as the reference energy (C 1s = 284.6 eV). Raman spectra were collected using a Renishaw inVia Raman spectrometer system (Gloucestershire, UK) equipped with a Leica DMLB microscope (Wetzlar, Germany) and a Renishaw He–Ne laser source that produced 17 mW at λ = 633 nm. The N$_2$-sorption measurement was carried out at 77 K with a Micromeritics 3Flex Surface Characterization Analyser.

Cell assembly and electrochemical testing

The electrodes were prepared by dispersing the as-prepared material (80 wt%) and poly (Vinylidene fluoride) binder (PVDF, 20 wt%) in *N*-methyl-2-pyrrolidone (NMP) to form a slurry. The resultant slurry was pasted onto copper foil using a doctor blade and dried in a vacuum oven for 12 h, followed by pressing at 200 kg cm^{-2}. The loading weight of the electro-active material is around 1.1 mg cm^{-2}. Electrochemical measurements were carried out using two electrode coin cells with Na metal as counter and reference electrodes and the glass micro-

fiber (Whatman) as the separator. The CR2032-type coin cells were assembled in an argon-filled glove box (UniLab, Mbraun, Germany). The electrolyte solution was 1 M $NaClO_4$ dissolved in a mixture of ethylene carbonate (EC) and propylene carbonate (PC) with a volume ratio of 1 : 1 with a 5 vol% addition of fluoroethylene carbonate (FEC). All the capacities were calculated based on the mass of the composites. Cyclic voltammetry (CV) was conducted on a CHI 660C instrument between 0.01 and 3 V *vs.* Na/Na^+ at room temperature. For the electrochemical impedance spectroscopy (EIS) measurement, the excitation amplitude applied to the cells was 5 mV. The charge–discharge measurements were performed at ambient temperature at different current densities in the voltage range from 0.01 and 3 V *vs.* Na/Na^+.

Results and discussion

In the present study, a facile hydrothermal method has been developed to prepare SnO_2/NG nanohybrids using urea as the nitrogen precursor (Fig. S1, ESI†). $SnCl_4$ was mixed with GO aqueous suspension first. Because of the electrostatic interaction between Sn^{4+} anions and negatively charged GO, Sn^{4+}/GO hybrids can be readily obtained in this step. The Sn^{4+}/GO hybrids, together with urea, were then subjected to hydrothermal treatment. During hydrothermal treatment, NH_3 can be released slowly from urea, which can be used as nitrogen-doping agent in the confined space.[36] The low-temperature incorporation of nitrogen heteroatoms into graphene networks was achieved by the reason that the hydrothermal condition, *i.e.*, 180 °C and autogenous pressure, promoted the reaction between basic NH_3 and oxygen functionalities (such as carboxylic acid and hydroxyl species) and finally enabled the *in situ* doping of nitrogen.[36] The oxygen-containing groups on GO, such as carboxyl, hydroxyl and epoxy groups, act as the nucleation and growth sites, and homogeneously dispersed SnO_2 nanocrystals formed consequently. The nitrogen dopants can also interact with the Sn^{4+}, providing additional active sites for SnO_2 formation, which results in a strong coupling between metal species and N-doped graphene.[37,38] Our synthesis protocol avoids high-temperature nitridation of graphene. For comparison, we prepared SnO_2/G using the same procedure without the addition of urea as a benchmark to investigate the nitrogen-doping effects of SnO_2/NG nanocomposites as anode materials for SIBs. TGA curves in Fig. S2 (ESI†) suggest that SnO_2/G has the same SnO_2 weight ratio as SnO_2/NG (47.0%).

The crystal structure of SnO_2/NG and SnO_2/G nanocomposites has been characterized by X-ray diffraction (XRD), as shown in Fig. 1(a). The XRD patterns show diffraction peaks at 26.6°, 33.7°, 37.9°, 51.8° and 65.3°, which can be well indexed to the pure tetragonal rutile phase of SnO_2 crystals with the space group of $P42/mnm$ (JCPDS card no. 41-1445). Because of the balance between the depletion of oxygen-containing groups and the introduction of nitrogen heteroatoms,[36] there should be no big difference of the total sites for the growth of
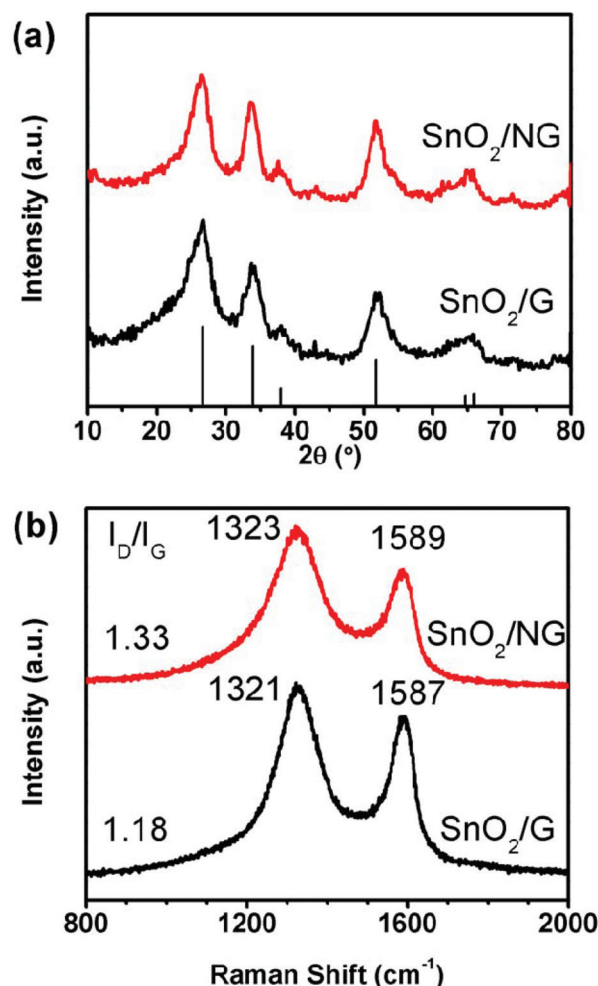

Fig. 1 (a) XRD patterns of SnO_2/NG and SnO_2/G composites. (b) Raman spectra of SnO_2/NG and SnO_2/G composites in the range of 800–2000 cm^{-1}.

SnO_2 nucleus between NG and graphene, which can be reflected by the XRD results. As calculated by Scherrer equation, the crystalline size of SnO_2 in SnO_2/NG (1.6 nm) is similar to that in SnO_2/G (1.4 nm). The microstructure of NG has been investigated by Raman spectroscopy, as presented by Fig. 1(b). Two characteristic peaks at 1323 and 1589 cm^{-1} can be observed in the range of 800–2000 cm^{-1}, corresponding to the D band and G band of NG, respectively. Compared to the SnO_2/G counterpart, the as-synthesized SnO_2/NG nanohybrids exhibit an upshift of the D band and G band (from 1321 cm^{-1} to 1323 cm^{-1} for D band and from 1587 cm^{-1} to 1589 cm^{-1} for G band). This may originate from structural distortion of graphene caused by the different bond distances of C–C and C–N.[29] Moreover, SnO_2/NG shows a higher I_D/I_G (intensity ratio between D band and G band) value (1.33) than that of SnO_2/G composites (1.18), which suggests a more disordered structure for NG than graphene owing to the introduction of N heteroatoms in graphene networks. Both the shift of band positions and the larger I_D/I_G value indicate that nitrogen heteroatoms

have been successfully inserted into graphene by the hydro-thermal method.

TEM has been used to investigate the microstructures of the as-obtained SnO$_2$/NG and SnO$_2$/G, as depicted in Fig. 2. The crumpling of NG layers, as observed in Fig. 2(a), is attributed to defective structures formed during the oxidation-reduction procedure for the synthesis of NG, which is in agreement with the Raman result. On the other hand, it can be clearly seen that ultrafine SnO$_2$ nanocrystals have been successfully loaded onto the surface of NG after hydrothermal treatment. A high-resolution TEM image of SnO$_2$/NG nanohybrids is shown in Fig. 2(c), from which it can be observed that the crystal plane distance is 0.33 and 0.26 nm, corresponding to the (110) and (101) face of tetragonal SnO$_2$, respectively. The particle size distribution of SnO$_2$ in the as-prepared SnO$_2$/NG nanohybrids is shown in Fig. 2(e). And the average particle size of SnO$_2$ is calculated to be 4.7 nm. The morphology of SnO$_2$/G composites (Fig. 2(b, d and f)) is similar to that of SnO$_2$/NG, and the average particle size of SnO$_2$ in SnO$_2$/G composites is 4.0 nm. Fig. S3 (ESI†) shows the nitrogen sorption isotherms of SnO$_2$/NG and SnO$_2$/G composites at 77 K. Both the two adsorption–desorption curves can be classified as the typical type-IV isotherm with an H$_1$-type loop hysteresis.[39] It is calculated that the BET surface area of SnO$_2$/G and SnO$_2$/NG material is very close, which is 215 and 206 m^2 g^{-1}, respectively. It is calculated that the average pore diameter of SnO$_2$/NG nanocomposites is 3.0 nm, approximating to that of SnO$_2$/G nanocomposites (3.3 nm).

The X-ray photoelectron spectroscopy (XPS) experiments provide further evidences of the chemical configuration of nitrogen species and the interaction between SnO$_2$ nanocrystals and the NG matrix. From the survey XPS scan in Fig. 3(a), it can be identified that the as-obtained SnO$_2$/NG composites are composed of C, N, O and Sn elements. No other signals can be found, which implies the purity of the as-synthesized samples. The high resolution C 1s spectrum is shown in Fig. 3(b), which can be fitted into five peaks at 284.6 eV (graphitic carbon), 285.4 eV (N–C$_{sp2}$), 286.7 eV (N–C$_{sp3}$), 288.7 eV (C=O) and 291.0 eV (shake-up satellite peak due to π–π* transitions in aromatic systems).[40] The overwhelming percentage of graphitic carbon suggests the graphitized nature of the NG in SnO$_2$/NG composites. The nitrogen bonding configuration can be obtained from the high resolution N 1s spectrum, as shown in Fig. 3(c). The result from the curve fitting indicates the presence of four different types of nitrogen species bonded to carbon in the composite: pyridinic N (398.3 eV), pyrrolic N (399.8 eV), graphitic N (400.9 eV) and oxidic N of pyridinic-N
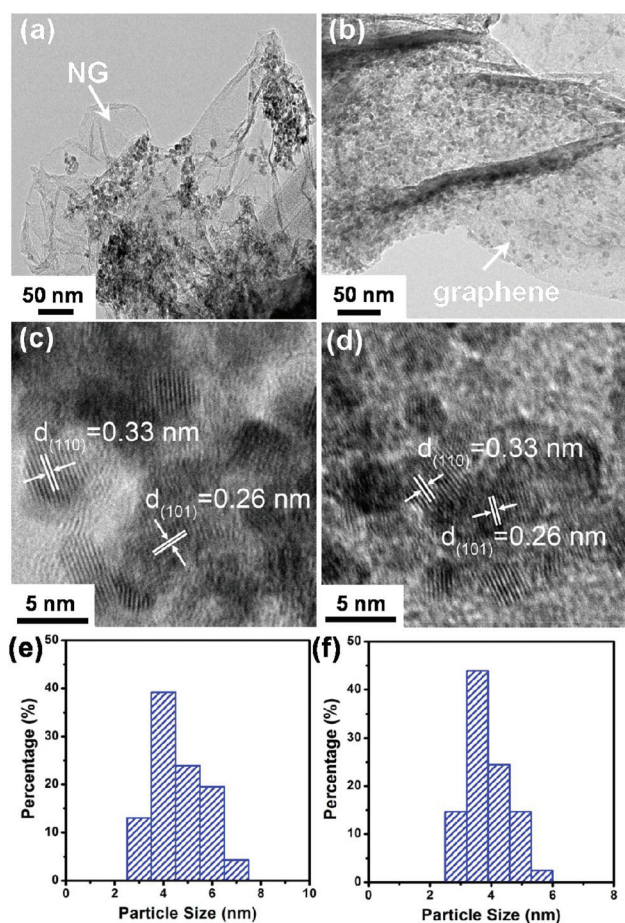

Fig. 2 Medium-magnification TEM image, high-resolution TEM image, SnO$_2$ particle size distribution of SnO$_2$/NG nanohybrids (a, c, and e) and SnO$_2$/G composites (b, d, and f).
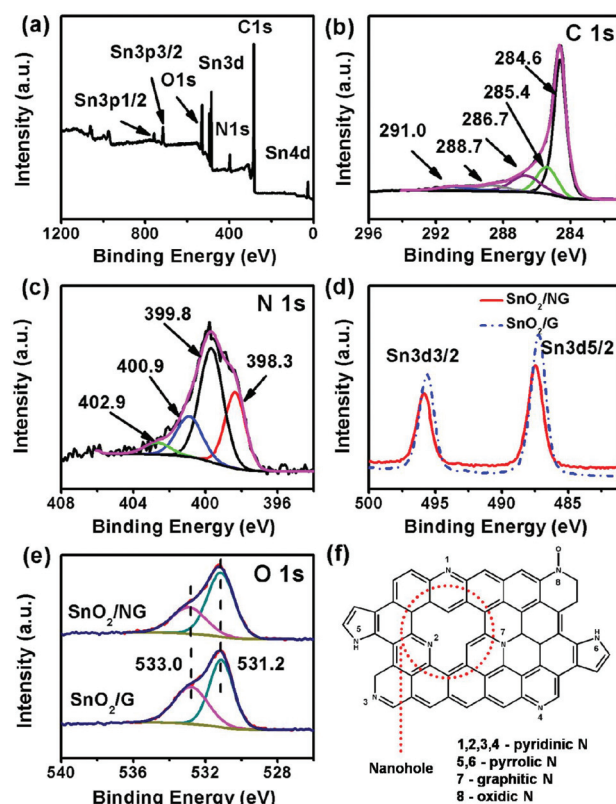

Fig. 3 XPS analysis of SnO$_2$/NG and SnO$_2$/G composites: (a) the survey spectrum, (b) high-resolution spectrum of C 1s, (c) N 1s spectrum, (d) XPS Sn 3d spectra, and (e) O 1s spectra. (f) Schematic illustration of different nitrogen species in NG.

(402.9 eV).[41–45] Notably, the pyridinic and pyrrolic N species are dominant in the composite, indicating that nitrogen heteroatoms are mainly resident at the edges and/or the nanoholes of the two-dimensional graphene (Fig. 3(f)). It is calculated that the total amount of nitrogen doped in NG is *ca.* 6.2 at%. As shown in Fig. 3(d), the binding energy of $Sn \; 3d_{3/2}$ and $Sn \; 3d_{5/2}$ in SnO_2/G composite is 495.8 eV and 487.5 eV, respectively. In comparison, the location of the Sn XPS peaks in the SnO_2/NG composite shifts toward larger binding energy. Fig. 3(e) shows the O 1s XPS spectrum of the SnO_2/NG composites, which can be deconvoluted into two peaks. The peak at 531.2 eV is assigned to C=O groups or shoulder peak of O 1s in SnO_2, and the peak at 533.0 eV is ascribed to C–OH and/or C–O–C groups (hydroxyl and/or epoxy).[46–48] The O/C ratio in NG is 0.073, which is much lower than that in graphene (0.126) due to the replacement of N. The same O 1s binding energy of SnO_2/NG composites as that of SnO_2/G suggests that the different binding energy of Sn 3d in the as-prepared $SnO_2/$ NG compared to that in SnO_2/G does not originate from size effects or charge correction issues. The XPS results indicate that SnO_2 nanocrystals are effectively coupled with the NG scaffold due to the nitrogen-doping, which facilitates the electron transfer at the interface between SnO_2 and NG during repeated sodiation/de-sodiation processes as discussed in the following part.

The electrochemical reactions between SnO_2/NG and Na^+ have been investigated by cyclic voltammetry (CV), as shown in Fig. 4. It has been revealed by TEM studies that upon sodium-ion insertion into SnO_2, a displacement reaction occurs to form the amorphous Na_xSn nanoparticles dispersed in Na_2O matrix,[49] and SnO_2 nanocrystals can be reversed back to the original phase at the charge state.[50] In the first discharge process, the peaks in the region from 3.0 V to 1.0 V could be ascribed to the Na^+ insertion into SnO_2 crystals to form the $NaSnO_2$ intermediate phase.[50] A pair of cathodic and anodic peaks located at 0.9 V and 1.6 V can be clearly observed. Since

these two peaks can also be observed for the bare NG electrode (Fig. S4, ESI†), they can be ascribed to the interaction between Na^+ and impure atoms in the graphene network, such as O in residual oxygen-containing functional groups and N heteroatoms.[51] Because propylene carbonate (PC) decomposes at 0.7 V *vs.* Li/Li^+ and $E^\circ(Na/Na^+)$ is 0.33 V higher than $E^\circ(Li/Li^+)$,[52] it is plausible to assign the cathodic peak at 0.35 V to PC decomposition in the present Na^+ half-cell where the Na piece was used as reference electrode, forming a solid-electrolyte interphase (SEI) at the SnO_2/NG electrode.[53] Besides, the peaks from 0.7 V to 0.01 V are associated with the alloying reaction to form Na_xSn alloys embedded in the Na_2O matrix during the cathodic process in the first cycle. In addition, a pronounced sodium insertion peak can be observed at near 0.01 V in each cycle, which is analogue to lithium insertion in carbonaceous materials.[54]

The advantages of the as-prepared SnO_2/NG over SnO_2/G as anode materials for SIBs have been investigated by galvanostatic discharge/charge measurements in the voltage range of 0.01–3.0 V. As can be seen in Fig. S5 (ESI†), bare SnO_2 only delivers an initial reversible capacity of 153 mA h g^{-1}. The capacity dramatically drops to 38 mA h g^{-1} after 100 cycles at a current density of 20 mA g^{-1}. Both SnO_2/G and SnO_2/NG show higher reversible capacities than bare SnO_2. Particularly, in the 1st cycle, the SnO_2/G electrode delivers a discharge and charge capacity of 652 mA h g^{-1} and 225 mA h g^{-1}, respectively (Fig. 5(a)). SnO_2/NG nanohybrids show much higher capacities as anode materials for SIBs. As shown in Fig. 5(a), the initial reversible capacity of the SnO_2/NG electrode is 339 mA h g^{-1}, which is 114 mA h g^{-1} higher than that of SnO_2/G. The initial Coulombic efficiency of SnO_2/NG electrode is 43.6%. The 56.4% capacity loss of the SnO_2/NG electrode may be ascribed to the irreversible formation of the SEI layer on the electrode. According to previous investigations, the SEI is composed of inorganic and organic layers around the particles.[55,56] The organic layers can form and dissolve reversibly, which contributes to the reversible capacity. On the contrary, the formation of an inorganic layer is an irreversible process. Interestingly, it is noted that SnO_2/NG nanocomposites have a higher initial Coulombic efficiency than that of SnO_2/G (34.5%), which indicates that nitrogen incorporation is beneficial for the reversibility of the SnO_2/NG electrode. The cycling performances of SnO_2/NG and SnO_2/G are shown in Fig. 5(b). SnO_2/NG exhibits a universal superior electrochemical performance, compared with SnO_2/G, within 100 cycles at a current density of 20 mA g^{-1}. SnO_2/NG electrode delivers capacities of 305 and 283 mA h g^{-1} in the 50th and 100th cycle, which are higher than those of SnO_2/G electrode (207 and 188 mA h g^{-1}), as shown in Fig. S6.†

Fig. 6(a) shows the cycling performance of the SnO_2/NG nanohybrids at different current densities. The SnO_2/NG electrodes exhibit satisfying high rate performances. After 100 cycles, the SnO_2/NG anode still delivers high discharge capacities when cycled at different current densities: 238 mA h g^{-1} at 40 mA g^{-1}, 246 mA h g^{-1} at 80 mA g^{-1}, respectively. We also tested the multiple-step cycling characteristics of SnO_2/NG at
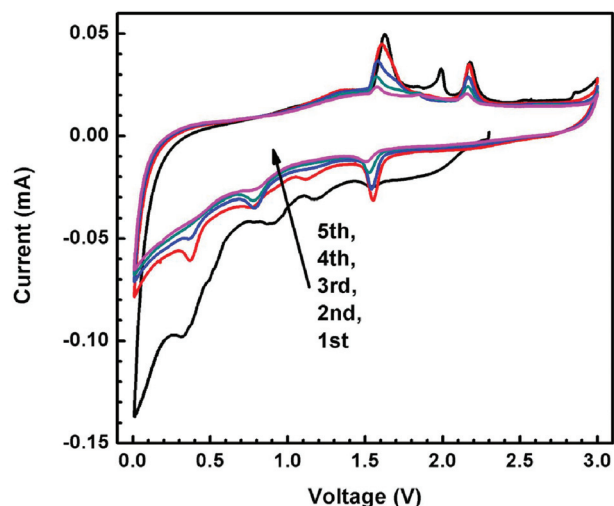

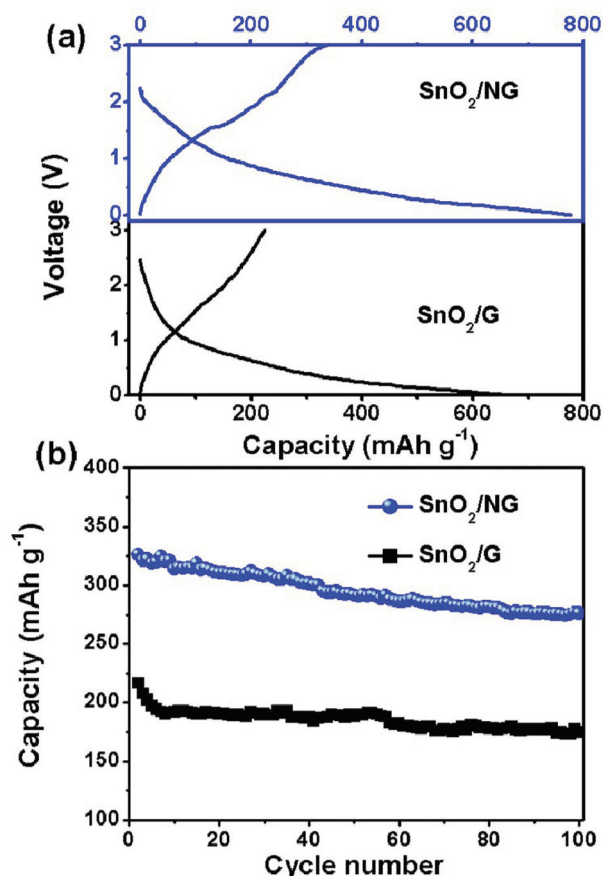Fig. 4 CV profiles of the SnO_2/NG composites at a scan rate of 0.1 mV s^{-1} between 0.01 and 3.0 V.

Fig. 5 (a) Galvanostatic charge–discharge profiles of the SnO$_2$/NG and SnO$_2$/G composites. (b) Cycling performance of SnO$_2$/NG and SnO$_2$/G composites at a current density of 20 mA g^{-1} from the second cycle.

Fig. 6 (a) Cycling performance of SnO$_2$/NG composites at current densities of 40 and 80 mA g^{-1} from the second cycle. (b) Rate performance of SnO$_2$/NG at different current densities.

20, 40, 80, 160, 320, 640 mA g^{-1} and 320, 160, 80, 40, 20 mA g^{-1}. As depicted in Fig. 6(b), the SnO$_2$/NG nanocomposite electrode shows an excellent high rate performance. At a current density of 640 mA g^{-1}, SnO$_2$/NG can still deliver a capacity of 170 mA h g^{-1}, which is preferable for high power density devices. When the current density reversed to the lower value (20 mA g^{-1}), the electrode recovered substantial capacities without obvious capacity decay.

We experimentally observe that SnO$_2$/NG exhibits enhanced electrochemical performance for sodium-ion storage compared to the SnO$_2$/G counterpart. The TGA results, TEM analysis, and BET results clearly demonstrate that the electrochemical performance enhancement does not originate from either the loading ratio difference of SnO$_2$ or the morphology effect. Consequently, it is reasonable to conclude that the nitrogen dopants in the graphene structure contribute to the improved capacity of SnO$_2$/NG compared to the SnO$_2$/G counterpart for Na$^+$ storage. Firstly, it is theoretically and experimentally well known that N substitution can enhance Li-ion storage in pristine graphene by inducing surface defects and introducing heteroatomic N into the graphene structure, which can provide additional sites for Li$^+$ adsorption.[27,57–60] Similarly, NG matrix in SnO$_2$/NG nanocomposites could be
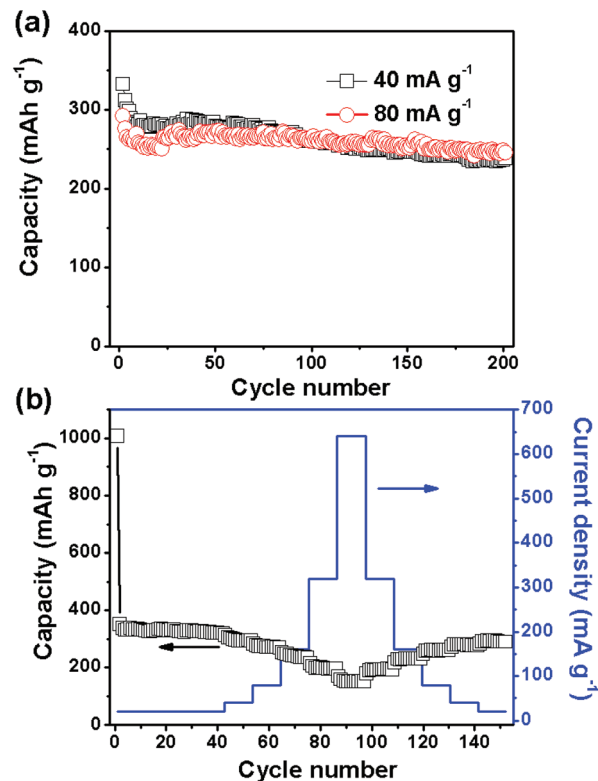
more active for Na$^+$ storage than the graphene matrix in SnO$_2$/G nanohybrids. As evidenced by Fig. 7(a), bare NG exhibits an enhanced capacity compared to graphene. In the first cycle, NG delivers a reversible capacity of 163 mA h g^{-1}, this value is 29 mA h g^{-1} higher than that of graphene. On the other hand, nitrogen-doping can enhance the electron transport properties of the SnO$_2$/NG electrode, as demonstrated by the Nyquist plots in Fig. 7(b). Both Nyquist plots are composed of a depressed semicircle in the moderate frequency region and a straight line in the low frequency region. Normally, the depressed semicircle is attributed to the charge transfer process. Apparently, the semicircle of SnO$_2$/NG is smaller than that of the SnO$_2$/G material, indicating that SnO$_2$/NG composites possess higher electron transfer efficiency. On the other hand, the low-frequency slope angle is 49° for SnO$_2$/NG negative electrode, whereas SnO$_2$/G has a slope angle of 38°. The much steeper straight line in the low frequency region suggests that a better Na-ion kinetics in SnO$_2$/NG electrode than in SnO$_2$/G electrode.[48] The improved Na-ion kinetics could be due to the higher electronegativity of NG than that of graphene.[61] The ac impedance spectra can be modeled by the modified Randles equivalent circuit presented in the inset in Fig. 7(b). R_e is the electrolyte resistance, CPE represents constant phase element, R_f is the resistance of the passivation film formed on the surface of the electrode, R_{ct} is the charge-transfer resistance, and Z_w is the Warburg impedance related
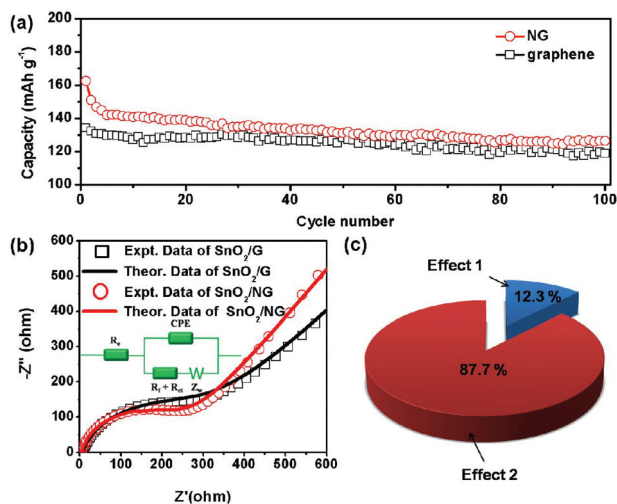
Fig. 7 (a) Cycling performance of graphene and NG at a current of 20 mA g^{-1}. (b) The Nyquist plots of the SnO$_2$/G and SnO$_2$/NG electrode, the inset shows the modeled equivalent circuit. (c) Contribution of different nitrogen-doping effects to the overall electrochemical performance enhancement of SnO$_2$/NG nanohybrids for SIBs compared to SnO$_2$/G, where Effect 1 is the increased electro-active sites within graphene matrix due to the nitrogen-doping and Effect 2 is the improved electron transfer efficiency within the SnO$_2$/NG electrode benefiting from nitrogen-dopants.

to the diffusion of Na$^+$ into the bulk of the electrodes. The kinetic parameters of SnO$_2$/G and SnO$_2$/NG electrodes are shown in Table S1.† The values of R_e and the combined surface film and charge transfer resistance $R_f + R_{ct}$ for the SnO$_2$/NG electrode are 4.6 and 254.8 Ω, which are lower than those for the SnO$_2$/G electrode (6.6 and 301.4 Ω). This indicates that nitrogen-doping of graphene is beneficial for the high conductivity for electron and charge transfer with low electrolyte resistance. As illustrated by Fig. 8, the improved electron transfer efficiency within the SnO$_2$/NG electrode can be ascribed to the following nitrogen-doping effects: (1) graphitic N can provide a strong n-doping effect, which contributes to the conductivity enhancement.[7,28,34,62] (2) As revealed by the XPS analysis, SnO$_2$ nanocrystals are effectively bonded to NG scaffold. As a result, the electron transfer efficiency at the interface between SnO$_2$ and matrix is improved because a good adhesion and electrical contact between SnO$_2$ and NG is achieved. Both the increased electro-active sites within graphene matrix and the improved electron transfer efficiency
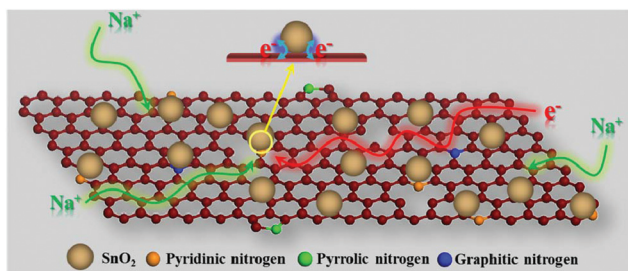
due to nitrogen-doping make SnO$_2$/NG favorable for electrochemical Na$^+$ storage compared to SnO$_2$/G. However, taking account of the NG weight ratio in the as-prepared SnO$_2$/NG nanohybrids, the increased electro-active sites within graphene matrix due to nitrogen-doping only have a contribution of 14 mA h g^{-1} (29 mA h g^{-1} × W_{NG} = 14 mA h g^{-1}, where W_{NG} is the weight ratio of NG in the composite), which accounts for 12.3% of the overall capacity enhancement of the SnO$_2$/NG electrode compared to the SnO$_2$/G counterpart (114 mA h g^{-1}), as depicted in Fig. 7(c). Consequently, the important role of nitrogen-doping should lie in improving the electron transfer efficiency within the SnO$_2$/NG electrode during sodiation/de-sodiation processes.

We carried out post-mortem SEM analysis on the SnO$_2$/NG electrode to check the integrity of the electrode. Fig. S7† shows the SEM images of the SnO$_2$/NG composite electrode after 100 cycles. Neither pulverization nor peeling off of SnO$_2$ can be observed due to the small size of SnO$_2$ nanoparticles and the mechanical resilience of NG nanosheets, which can effectively buffer the big volume expansion during repeated charge/discharge processes. As a result, SnO$_2$/NG composites show good cycling stability as anode materials for SIBs.

Conclusions

In summary, SnO$_2$/NG nanohybrids have been successfully prepared by a facile hydrothermal method using urea as nitrogen-doping agents. The as-synthesized SnO$_2$/NG material contains ultrafine SnO$_2$ nanocrystals with an average particle size of 4.7 nm. When applied as anode material for sodium-ion batteries, the as-prepared SnO$_2$/NG nanohybrids exhibit an enhanced electrochemical performance for SIBs compared to the SnO$_2$/G counterpart. A comparison between SnO$_2$/NG nanohybrids and the SnO$_2$/G counterpart has been conducted in a reasonable framework to manifest the inherent nitrogen-doping effects for the enhancement of sodium-ion storage performance. It is found that although nitrogen-doping can improve the Na$^+$ storage capacity within the graphene networks by increasing electro-active sites, its contribution to the overall electrochemical performance enhancement of the SnO$_2$/NG compared to the SnO$_2$/G counterpart is limited. While the improvement of the electron transfer efficiency within the electrode due to nitrogen-doping plays the major role for the enhancement of the electro-activity of SnO$_2$/NG. This work highlights that nitrogen-dopants in graphene networks can effectively mediate the electron transfer between SnO$_2$ and NG, thereby offering fundamental concepts to rationally design graphene-based electrode materials with higher performance for SIBs.

Acknowledgements

Fig. 8 SnO$_2$/NG nanohybrids as anode materials for SIBs.

Notes and references

1 B. Ellis, W. Makahnouk, Y. Makimura, K. Toghill and L. Nazar, *Nat. Mater.*, 2007, **6**, 749–753.

2 S. Komaba, W. Murata, T. Ishikawa, N. Yabuuchi, T. Ozeki, T. Nakayama, A. Ogata, K. Gotoh and K. Fujiwara, *Adv. Funct. Mater.*, 2011, **21**, 3859–3867.

3 Y. Cao, L. Xiao, M. L. Sushko, W. Wang, B. Schwenzer, J. Xiao, Z. Nie, L. V. Saraf, Z. Yang and J. Liu, *Nano Lett.*, 2012, **12**, 3783–3787.

4 Y. Liu, Y. Xu, Y. Zhu, J. N. Culver, C. A. Lundgren, K. Xu and C. Wang, *ACS Nano*, 2013, **7**, 3627–3634.

5 Y. Sun, L. Zhao, H. Pan, X. Lu, L. Gu, Y.-S. Hu, H. Li, M. Armand, Y. Ikuhara, L. Chen and X. Huang, *Nat. Commun.*, 2013, **4**, 1870.

6 H. Zhu, Z. Jia, Y. Chen, N. Weadock, J. Wan, O. Vaaland, X. Han, T. Li and L. Hu, *Nano Lett.*, 2013, 3093–3100.

7 P. Nie, Y. Zhu, L. Shen, G. Pang, G. Xu, S. Dong, H. Dou and X. Zhang, *J. Mater. Chem. A*, 2014, **2**, 18606–18612.

8 Y. Kim, K.-H. Ha, S. M. Oh and K. T. Lee, *Chem. – Eur. J.*, 2014, **20**, 11980–11992.

9 N. Yabuuchi, K. Kubota, M. Dahbi and S. Komaba, *Chem. Rev.*, 2014, **114**, 11636–11682.

10 J. Qian, X. Wu, Y. Cao, X. Ai and H. Yang, *Angew. Chem., Int. Ed.*, 2013, **52**, 4633–4636.

11 W. Li, S.-L. Chou, J.-Z. Wang, J. H. Kim, H.-K. Liu and S.-X. Dou, *Adv. Mater.*, 2014, **26**, 4037–4042.

12 J. Qian, Y. Xiong, Y. Cao, X. Ai and H. Yang, *Nano Lett.*, 2014, **14**, 1865–1869.

13 Y. Liu, N. Zhang, L. Jiao, Z. Tao and J. Chen, *Adv. Funct. Mater.*, 2015, **25**, 214–220.

14 X. Xie, D. Su, S. Chen, J. Zhang, S. Dou and G. Wang, *Chem. – Asian J.*, 2014, **9**, 1611–1617.

15 T. Zhou, W. K. Pang, C. Zhang, J. Yang, Z. Chen, H. K. Liu and Z. Guo, *ACS Nano*, 2014, **8**, 8323–8333.

16 Y. Liu, H. Kang, L. Jiao, C. Chen, K. Cao, Y. Wang and H. Yuan, *Nanoscale*, 2015, **7**, 1325–1332.

17 J. Qian, Y. Chen, L. Wu, Y. Cao, X. Ai and H. Yang, *Chem. Commun.*, 2012, **48**, 7070–7072.

18 Y. Zhu, X. Han, Y. Xu, Y. Liu, S. Zheng, K. Xu, L. Hu and C. Wang, *ACS Nano*, 2013, **7**, 6378–6386.

19 D. Y. W. Yu, P. V. Prikhodchenko, C. W. Mason, S. K. Batabyal, J. Gun, S. Sladkevich, A. G. Medvedev and O. Lev, *Nat. Commun.*, 2013, **4**, 2922–2928.

20 L. David, R. Bhandavat and G. Singh, *ACS Nano*, 2014, **8**, 1759–1770.

21 B. Qu, C. Ma, G. Ji, C. Xu, J. Xu, Y. S. Meng, T. Wang and J. Y. Lee, *Adv. Mater.*, 2014, **26**, 3854–3859.

22 M.-Q. Yang, N. Zhang, M. Pagliaro and Y.-J. Xu, *Chem. Soc. Rev.*, 2014, **43**, 8240–8254.

23 Y. Zhang, Z.-R. Tang, X. Fu and Y.-J. Xu, *ACS Nano*, 2011, **5**, 7426–7435.

24 N. Zhang, Y. Zhang and Y.-J. Xu, *Nanoscale*, 2012, **4**, 5792–5813.

25 M.-Q. Yang and Y.-J. Xu, *Phys. Chem. Chem. Phys.*, 2013, **15**, 19102–19118.

26 N. Zhang, M.-Q. Yang, Z.-R. Tang and Y.-J. Xu, *ACS Nano*, 2014, **8**, 623–633.

27 A. L. M. Reddy, A. Srivastava, S. R. Gowda, H. Gullapalli, M. Dubey and P. M. Ajayan, *ACS Nano*, 2010, **4**, 6337–6342.

28 D. Usachov, O. Vilkov, A. Grüneis, D. Haberer, A. Fedorov, V. K. Adamchuk, A. B. Preobrajenski, P. Dudin, A. Barinov, M. Oehzelt, C. Laubschat and D. V. Vyalikh, *Nano Lett.*, 2011, **11**, 5401–5407.

29 Z.-S. Wu, W. Ren, L. Xu, F. Li and H.-M. Cheng, *ACS Nano*, 2011, **5**, 5463–5471.

30 Z.-R. Tang, Y. Zhang, N. Zhang and Y.-J. Xu, *Nanoscale*, 2015, DOI: 10.1039/C1034NR05879H.

31 H.-G. Wang, Z. Wu, F.-L. Meng, D.-L. Ma, X.-L. Huang, L.-M. Wang and X.-B. Zhang, *ChemSusChem*, 2013, **6**, 56–60.

32 H. A. Cha, H. M. Jeong and J. K. Kang, *J. Mater. Chem. A*, 2014, **2**, 5182–5186.

33 G. Qin, X. Zhang and C. Wang, *J. Mater. Chem. A*, 2014, **2**, 12449–12458.

34 Z. Wang, L. Qie, L. Yuan, W. Zhang, X. Hu and Y. Huang, *Carbon*, 2013, **55**, 328–334.

35 W. S. Hummers and R. E. Offeman, *J. Am. Chem. Soc.*, 1958, **80**, 1339.

36 L. Sun, L. Wang, C. Tian, T. Tan, Y. Xie, K. Shi, M. Li and H. Fu, *RSC Adv.*, 2012, **2**, 4498–4506.

37 X. Xie, J. Long, J. Xu, L. Chen, Y. Wang, Z. Zhang and X. Wang, *RSC Adv.*, 2012, **2**, 12438–12446.

38 J. Duan, S. Chen, S. Dai and S. Z. Qiao, *Adv. Funct. Mater.*, 2014, **24**, 2072–2078.

39 K. S. W. Sing, D. H. Everett, R. A. W. Haul, L. Moscou, R. A. Pierotti, J. Rouquérol and T. Siemieniewska, *Pure Appl. Chem.*, 1985, **57**, 603–619.

40 X. Meng, H. Cui, J. Dong, J. Zheng, Y. Zhu, Z. Wang, J. Zhang, S. Jia, J. Zhao and Z. Zhu, *J. Mater. Chem. A*, 2013, 9469–9476.

41 J. Casanovas, J. M. Ricart, J. Rubio, F. Illas and J. M. Jiménez-Mateos, *J. Am. Chem. Soc.*, 1996, **118**, 8071–8076.

42 B. Guo, Q. Liu, E. Chen, H. Zhu, L. Fang and J. R. Gong, *Nano Lett.*, 2010, **10**, 4975–4980.

43 J. Jin, X. Fu, Q. Liu, Y. Liu, Z. Wei, K. Niu and J. Zhang, *ACS Nano*, 2013, 4764–4773.

44 Y. Jiao, Y. Zheng, M. Jaroniec and S. Z. Qiao, *J. Am. Chem. Soc.*, 2014, **136**, 4394–4403.

45 Y. Zheng, Y. Jiao, Y. Zhu, L. H. Li, Y. Han, Y. Chen, A. Du, M. Jaroniec and S. Z. Qiao, *Nat. Commun.*, 2014, **5**, 3783.

46 S. D. Gardner, C. S. K. Singamsetty, G. L. Booth, G.-R. He and C. U. Pittman Jr., *Carbon*, 1995, **33**, 587–595.

47 W. Lv, D.-M. Tang, Y.-B. He, C.-H. You, Z.-Q. Shi, X.-C. Chen, C.-M. Chen, P.-X. Hou, C. Liu and Q.-H. Yang, *ACS Nano*, 2009, **3**, 3730–3736.

48 G. Zhou, D.-W. Wang, L.-C. Yin, N. Li, F. Li and H.-M. Cheng, *ACS Nano*, 2012, **6**, 3214–3223.

49 M. Gu, A. Kushima, Y. Shao, J.-G. Zhang, J. Liu, N. D. Browning, J. Li and C. Wang, *Nano Lett.*, 2013, **13**, 5203–5211.

50 D. Su, C. Wang, H. Ahn and G. Wang, *Phys. Chem. Chem. Phys.*, 2013, **15**, 12543–12550.

51 Y.-X. Wang, S.-L. Chou, H.-K. Liu and S.-X. Dou, *Carbon*, 2013, **57**, 202–208.

52 Y. Marcus, *Pure Appl. Chem.*, 1985, **57**, 1129–1132.

53 K. Tang, L. Fu, R. J. White, L. Yu, M.-M. Titirici, M. Antonietti and J. Maier, *Adv. Energy Mater.*, 2012, **2**, 873–877.

54 J. Dahn, T. Zheng, Y. Liu and J. Xue, *Science*, 1995, **270**, 590–593.

55 P. Poizot, S. Laruelle, S. Grugeon and J.-M. Tarascon, *J. Electrochem. Soc.*, 2002, **149**, A1212–A1217.

56 K. Edström, T. Gustafsson and J. O. Thomas, *Electrochim. Acta*, 2004, **50**, 397–403.

57 X. Li, D. Geng, Y. Zhang, X. Meng, R. Li and X. Sun, *Electrochem. Commun.*, 2011, **13**, 822–825.

58 X. Wang, X. Cao, L. Bourgeois, H. Guan, S. Chen, Y. Zhong, D.-M. Tang, H. Li, T. Zhai, L. Li, Y. Bando and D. Golberg, *Adv. Funct. Mater.*, 2012, **22**, 2682–2690.

59 X. Wang, W. Tian, D. Liu, C. Zhi, Y. Bando and D. Golberg, *Nano Energy*, 2013, **2**, 257–267.

60 X. Wang, Q. Weng, X. Liu, X. Wang, D.-M. Tang, W. Tian, C. Zhang, W. Yi, D. Liu, Y. Bando and D. Golberg, *Nano Lett.*, 2014, **14**, 1164–1171.

61 F. Zheng, Y. Yang and Q. Chen, *Nat. Commun.*, 2014, **5**, 5261.

62 L. Fu, K. Tang, K. Song, P. A. van Aken, Y. Yu and J. Maier, *Nanoscale*, 2014, **6**, 1384–1389.